Aerosol hygroscopicity over the South-East Atlantic Ocean during the biomass burning season: Part I – From the perspective of scattering enhancement

Lu Zhang[1,2], Michal Segal-Rozenhaimer[1,3,4*], Haochi Che[2,5*], Caroline Dang[3,4], Junying Sun[6], Ye Kuang[7,8], Paola Formenti[9], Steven G. Howell[10]

[1]Department of Geophysics, Porter School of the Environment and Earth Sciences, Tel Aviv University, Tel Aviv, Israel

[2]Department of Environmental Science, Aarhus University, Roskilde, Denmark

[3]Bay Area Environmental Research Institute, Moffett Field, California, USA

[4]NASA Ames Research Center, Moffett Field, California, USA

[5]Department of Geosciences, University of Oslo, Oslo, Norway

[6]State Key Laboratory of Severe Weather & Key Laboratory of Atmospheric Chemistry, Chinese Academy of Meteorological Sciences, Beijing, China

[7]Institute for Environmental and Climate Research, Jinan University, Guangzhou, China

[8]Guangdong-Hongkong-Macau Joint Laboratory of Collaborative Innovation for Environmental Quality, Guangzhou, China

[9]Université Paris Cité and Univ Paris Est Creteil, CNRS, LISA, Paris, France

[10]Department of Oceanography, University of Hawai'i at Mānoa, Honolulu, USA

Correspondence: Michal Segal-Rozenhaimer (segalrozenhaimer@baeri.org) and Haochi Che (haochi.che@geo.uio.no)

Abstract

Aerosol hygroscopicity plays a vital role in aerosol radiative forcing. One key parameter describing hygroscopicity is the scattering enhancement factor, *f*(RH), defined as the ratio of the scattering coefficient at humidified relative humidity (RH) to its dry value. Here, we utilize the *f*(80%) from ORACLES 2016 and 2018 airborne measurements to investigate the hygroscopicity of aerosols, its vertical distribution, its relationship with chemical composition, and its sensitivity to organic aerosol (OA) hygroscopicity over the South-East Atlantic (SEA) Ocean during the biomass burning (BB) season.

We found that aerosol hygroscopicity remains steady above 2 km, with a mean *f*(80%) of 1.40±0.17. Below 2 km, aerosol hygroscopicity increases with decreasing altitude, with a mean *f*(80%) of 1.51±0.22, consistent with higher values of BB aerosol hygroscopicity found in the literature. The hygroscopicity parameter of OA (κ_{OA}) is retrieved from the Mie model with a mean value of 0.11±0.08, which is in the middle to upper range compared to literature. Higher OA hygroscopicity is related to aerosols that are more aged, oxidized, and present at lower altitudes. The enhanced BBA hygroscopicity at lower altitudes is mainly due to a lower OA fraction, increased sulphate fraction, and greater κ_{OA} at lower altitudes.

We propose a parameterization that quantifies *f*(RH) with chemical composition and κ_{OA} based on Mie simulation of internally mixed OA-$(NH_4)_2SO_4$-BC mixture. The good agreement between the predictions and the ORACLES measurements implies that the aerosols in the SEA during the BB season can be largely represented by the OA-$(NH_4)_2SO_4$-BC internal mixture with respect to the *f*(RH) prediction. The sensitivity of *f*(RH) to κ_{OA} indicates that applying a constant κ_{OA} is only suitable when the OA fraction is low and κ_{OA} shows limited variation. However, in situations deviating these two criteria, κ_{OA} can notably impact scattering

coefficients and aerosol radiative effect; therefore, accounting for κ_{OA} variability is recommended.

Keywords: hygroscopicity, biomass burning aerosol, chemical composition, κ_{OA}, Atlantic, airborne measurements, parameterization

1 Introduction

Aerosol hygroscopicity is an important physicochemical property of atmospheric aerosols, representing the extent to which particles take up water when exposed to a certain relative humidity (RH) (Covert et al., 1972). Key parameters describing aerosol hygroscopicity include the scattering enhancement factor, f(RH), which represents the enhancement of the aerosol light-scattering coefficient as a function of RH (Carrico et al., 2003), and κ, the hygroscopicity parameter, whose value is defined by its effect on the water activity of the solution (Petters and Kreidenweis, 2007). Water uptake will increase the size and the mass of hygroscopic aerosols, alter their refractive index, enhance the scattering ability, and ultimately influence the single scattering albedo and aerosol radiative forcing (Cotterell et al., 2017; Titos et al., 2021; Zieger et al., 2013). Furthermore, hygroscopicity affects aerosols' ability to act as CCN (cloud condensation nuclei) and ice nuclei, and further influences cloud properties and precipitation (Cai et al., 2021; Che et al., 2017; Ervens et al., 2007). Climate model results show that even a modest change in κ_{OA} (κ of organic aerosols) can lead to significant changes in CCN, droplet number concentration, and aerosol radiative effects (Liu and Wang, 2010; Rastak et al., 2017). The treatment of aerosol hygroscopicity is one of the key factors contributing to discrepancies between model simulations and observations and among model estimates (Burgos et al., 2020; Haywood et al., 2008; Reddington et al., 2019).

Africa emits ~ 1/3 of the Earth's annual biomass burning (BB) emissions (van der Werf et al., 2010), and its burned areas are increasing every year (Andela et al., 2017). Each Austral spring (July to October), the BB aerosols (BBA) from African fires are transported westward through the free troposphere (FT) over the persistent stratocumulus cloud deck in the South-East Atlantic (SEA), and eventually subside into the marine boundary layer (MBL) (Redemann et al., 2021). BBA undergo atmospheric processing during transport, altering their chemical composition, oxidation extent, particle polarity, molecular weight, volatility, and solubility

(Rastak et al., 2017), making the hygroscopicity highly variable. Laboratory studies show that minutes-old BBA are more hygroscopic than hour-old BBA (Day et al., 2006), while the hygroscopicity of BBA transported for more than several days in the SEA region remains an area of investigation. Furthermore, these BBA mix with pristine aerosols and are subject to marine influences from the SEA, resulting in a distinct vertical variation of aerosol hygroscopicity.

The hygroscopicity of organic aerosol (OA), the dominant component of aerosols in most cases, is poorly characterized due to its chemical complexity (Kuang et al., 2020a; Mei et al., 2013). Values of κ_{OA} can range from 0 for hydrophobic freshly emitted organics to approaching 1.0 for very hygroscopic amino acids (Kuang et al., 2020a; Petters et al., 2009; Zhang et al., 2007). BBOA are usually regarded as hydrophobic, while the mass fraction of aged BBOA show a positive correlation with κ_{OA} (Cerully et al., 2015; Kuang et al., 2021). Several studies have found a linear correlation between OA hygroscopicity and its oxidation level, commonly characterized by the oxygen-to-carbon (O/C) ratio or the fraction of total organic mass spectral signal at m/z 44 (f_{44}) (Lambe et al., 2011; Mei et al., 2013). However, this linear relationship is not always established, especially for secondary OA with a lower O/C ratio under sub-saturated conditions, for which solubility may play a more important role. In addition, studies show molecular weight, surface tension, and liquid-liquid phase separation are also related to the water affinity of OA (Liu et al., 2018; Rastak et al., 2017; Wang et al., 2019), all contributing to the complexity of OA hygroscopicity.

The ORACLES (ObseRvations of Aerosols above CLouds and their intEractionS) campaign (Redemann et al., 2021) provides a comprehensive observation of aerosols above the SEA Ocean with 4-12 days of transport from Africa fires, making it a valuable opportunity to investigate the hygroscopicity of aged BBA and their OA. In this paper, we first characterize the aerosol hygroscopicity and its vertical distribution over the SEA during the BB season, then

propose a parameterization relating aerosol hygroscopicity with chemical composition and k_{OA}, and finally evaluate the sensitivity of aerosol hygroscopicity to k_{OA}. Results are expected to provide a reference to the treatment of aerosol hygroscopicity in climate models and satellite retrievals, and to contribute to aerosol-cloud-interactions and radiative assessments in this climatically important SEA region.

2 Methods

2.1 Aircraft Instrumentation and Data Analysis

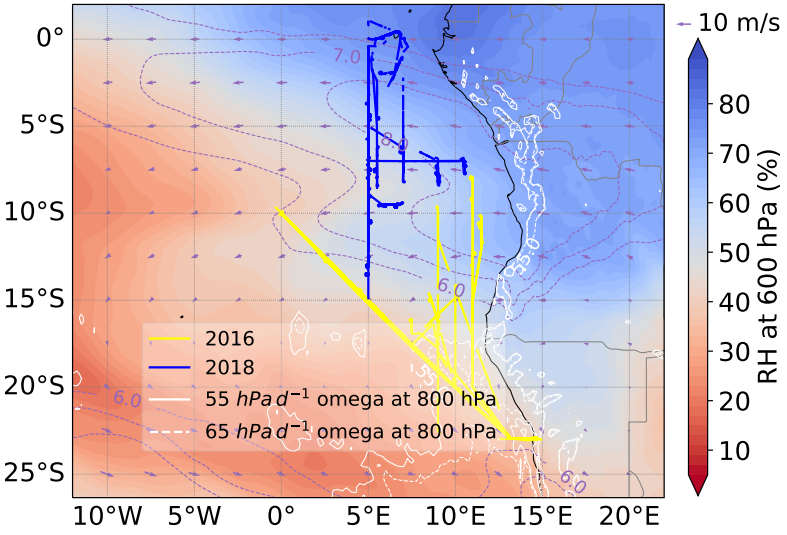

Figure 1. Flight tracks in 2016 and 2018 ORACLES campaigns. Map of October mean of ERA5 600 hPa RH overlaid by the 600 hPa zonal wind (purple contours; 6, 7, and 8 m s^{-1}), 600 hPa horizontal wind vector (purple arrows; m s^{-1}), and ORACLES flight tracks in 2016 (yellow) and 2018 (blue), respectively. White contours are the 2016 September mean vertical velocity, omega, at 800 hPa. Solid and dashed lines represent the subsidence of 55 and 65 hectopascals per day (hPa d^{-1}).

We analyzed airborne, in situ data measured over the SEA region from the ORACLES campaign performed in September 2016 and October 2018 (Redemann et al., 2021). The flight tracks are shown in Fig. 1. All instruments were deployed on the NASA P-3 aircraft. Aerosol

115 particles were introduced into the P-3 via the solid diffuser inlet. The inlet was operated
116 isokinetically by matching the flow rate to the external air flow velocity to within 5% (Dobracki
117 et al., 2023). This inlet was designed to effectively transfer particles up to 4.0 μm dry diameter
118 (McNaughton et al., 2007). The inner pipework was designed for minimal transport losses for
119 particles up to 4.0 μm using an online particle loss calculator (Aerosol Calculator,
120 https://tsi.com/getmedia/540a30fa-8444-49f6-814f-891495c70aa1/Aerocalc2001_1). Two
121 Radiance Research M903 integrating nephelometers (Nephs) were operating in parallel, one
122 (referred to as the 'reference Neph') under relatively dry conditions and the other (known as
123 the 'humidified Neph') maintained at ~80 % RH. Particles entering the reference Neph were
124 heated to the aircraft cabin temperature, significantly reducing their RHs in the Neph and
125 resulting in most particles having an RH below 35%. The humidified Neph was situated
126 downstream of a humidifier, which maintained the RH at the inlet of the Neph at ~80% within
127 a few percent, as detailed in Howell et al. (2006). The RH probes in M903 were corrected based
128 on lab calibrations and the RH errors are roughly 3%. The temperature errors are about 0.5℃.
129 Measurements were reported at 1 Hz. For the calculation of f(RH), data with a reference Neph
130 RH greater than 35% or a humidified Neph RH smaller than 76% were excluded. The
131 distribution of the RHs of both the reference and humidified Nephs used in this study are shown
132 in Fig. S3 in the supplementary material. Calibrations were performed in the field with
133 refrigerant R-134A (1,1,1,2-tetrafluoroethane). Truncation correction was performed for both
134 Nephs according to Anderson and Ogren (1998). All scattering coefficients and scattering
135 enhancement factors are reported at 540 nm wavelength.

136 The non-refractory submicron aerosol composition was provided by a High-Resolution
137 Time-of-Flight Aerosol Mass Spectrometer (HR-ToF-AMS, Aerodyne Research Inc.)
138 (Dobracki et al., 2023). The fragment analysis provided f_{44} and f_{60}, representing the fractions
139 of the OA mass spectrum signals at m/z=44 (mainly CO_2^+) and m/z=60 (mainly $C_2H_4O_2^+$),

140 respectively, in the total OA mass. The mass concentration of refractory BC was provided by
141 a single particle soot photometer (SP2, Droplet Measurement Technology, Sedlacek et al.,
142 2022).

143 The dry particle number size distribution (PNSD) of PM_1 was provided by an ultra-
144 high-sensitivity aerosol spectrometer (UHSAS, Droplet Measurement Technology). The
145 UHSAS measures particles between 60 and 1000 nm in optical diameter. It was calibrated with
146 polystyrene latex (PSL) spheres, whose real refractive index n is 1.572 at the UHSAS laser
147 wavelength (Howell et al., 2021). The UHSAS undersized particles in BB plumes; the
148 undersized data were corrected to mobility diameter according to Howell et al. (2021). The
149 PNSD of super-micron particles was measured by an aerodynamic particle sizer (APS). The
150 aerodynamic diameter of APS was converted to the volume equivalent diameter according to
151 DeCarlo et al. (2004). Particles were assumed to be spherical (shape factor = 1) with a density
152 of 1.5 g cm^{-3}. However, since the super-micron particles made a minimal contribution to the
153 total scattering coefficient, we have neglected the super-micron particles, and only UHSAS
154 measurements are used in this study. The minor contribution of super-micron particles to the
155 total scattering coefficients is described and illustrated in Section S1 and Fig. S1 in the
156 supplement. The aerosol/plume age was modelled with a two-week forecast using the Weather
157 Research and Aerosol Aware Microphysics (WRF-AAM) model (Thompson and Eidhammer,
158 2014). Carbon monoxide was tagged as tracer at the fire source, identified by a burned area
159 product from the moderate resolution imaging spectrometer with a 500 m spatial resolution.

160 All measurements were averaged to 15 s and adjusted to standard temperature and
161 pressure at 273.15 K and 1013 hPa. Data with scattering coefficient < 10 Mm^{-1} are not included.
162 The final measurements used in this study have an average RH of 79±0.5 % for the humidified
163 Neph and RH<30 % for the reference Neph. To ensure the influence of BB emissions, only
164 data with f_{60}>0.003 are considered (Cubison et al., 2011). This study analyzes measurements

from 21 flights, totaling approximately 134 flight hours after applying the abovementioned constraints.

2.2 Calculation of *f*(RH) and γ parameterization

The aerosol scattering enhancement factor, *f*(RH), is calculated as:

$$f(RH) = \frac{\sigma_{sp}(RH)}{\sigma_{sp}(RH_{ref})} \quad (1)$$

where σ_{sp}(RH) and σ_{sp}(RH_{ref}) represent the scattering coefficients at humidified and reference Neph RHs, respectively. Note the *f*(RH) only include those with reference Neph RHs equal to or smaller than 35 % to facilitate comparison with previous studies. For simplicity, we denote the *f*(RH) at the RH of humidified Neph as *f*(80%), despite the small variation of the RH in humidified Neph. The *f*(RH) is usually fitted to a γ parameterization to apply to a more extensive RH range (Sheridan et al., 2002; Titos et al., 2016):

$$f(RH) = \left(\frac{1 - RH/100}{1 - RH_{ref}/100}\right)^{-\gamma} \quad (2)$$

In our case, the γ was calculated with the RH and RH_{ref} using Eq. 2 since the *f*(RH) was only measured at a fixed RH.

2.3 Modeling of *f*(RH)

The *f*(RH) can be modeled with the Mie theory (Mie, 1908). The Python package PyMieScatt (Sumlin et al., 2018), an implementation of the Mie theory, was applied in this study. Inputs of PyMieScatt include PNSD and complex refractive index. Dry particles beyond PM_1 (particulate matter with an aerodynamic diameter less than 1 μm) are not included in this calculation, supported by their minor contribution to the total scattering, as discussed in Section S1 of the supplement. A volume mixing rule was used to calculate the refractive index. The volume of inorganic salts was converted from those of SO_4^{2-}, NO_3^-, and NH_4^+ from AMS following a modified ion-pairing scheme (Gysel et al., 2007; Zhang et al., 2022). Good

agreement has been achieved for calculated and measured scattering coefficients under dry conditions, which indicates good data quality and provides the basis for calculating *f*(RH) and retrieving $\kappa_{f(RH)}$. The comparison between calculated and measured scattering coefficients is shown in Fig. S4 in the supplement. By combining Mie model with the κ-Köhler theory, we can then calculate the scattering coefficients under humidified RH conditions. For more details of the calculation, refer to Zieger et al. (2013). Subsequently, *f*(RH) and γ can be obtained using Eq. 1 and 2. The theoretically calculated *f*(RH) in Sections 3.3.1 and 3.3.2 used an assumed PNSD and different chemical composition combinations. One assumed PNSD was used in these calculations due to its minor impact on *f*(RH), which has been discussed in detail in Section S2 in the supplement.

2.4 $\kappa_{f(RH)}$ retrieval and κ_{OA} calculation

The aerosol hygroscopicity parameter κ can be retrieved from *f*(RH), usually denoted as $\kappa_{f(RH)}$ (Chen et al., 2014). It can be regarded as the scattering coefficient weighted average κ (Kuang et al., 2021). Specifically, we iteratively adjust $\kappa_{f(RH)}$ to minimize the difference between the calculated and measured *f*(RH). Detailed descriptions of the retrieval procedure of $\kappa_{f(RH)}$ can be found in Chen et al. (2014).

According to Petters and Kreidenweis (Petters and Kreidenweis, 2007), the overall κ_{chem}, which is defined as the κ for the whole aerosol population, can also be calculated from various chemical compositions following the ZSR (Zdanovskii-Stokes-Robinso) mixing rule. Kuang et al. (2020b) thoroughly outlined in Section 3.3 that the $\kappa_{f(RH)}$ can accurately represent the κ_{chem} of PM_1. Therefore, the hygroscopicity parameter of OA, κ_{OA}, can be calculated as:

$$\kappa_{OA} = \frac{\kappa_{f(RH)} - (\sum_{i=inorg} \kappa_i \varepsilon_i + \kappa_{BC} \varepsilon_{BC})}{\varepsilon_{OA}}, \quad (3)$$

where *inorg* represents inorganic salts, which were derived from the SO_4^{2-}, NO_3^-, and NH_4^+ ions measured from AMS following a modified ion-pairing scheme (Gysel et al., 2007; Zhang

et al., 2022). The subscript *i* denotes each individual inorganic salt. ε represents the volume fraction of each component, calculated as the ratio of the volume of each component to the volume of PM_1. The PM_1 volume is computed as the sum of the volumes of inorganic salts, OA, and BC. The hygroscopic parameter κ and density used in this study can be found in Table S1.

3 Results and discussion

3.1 Overview of chemical compositions in 2016 and 2018 ORACLES

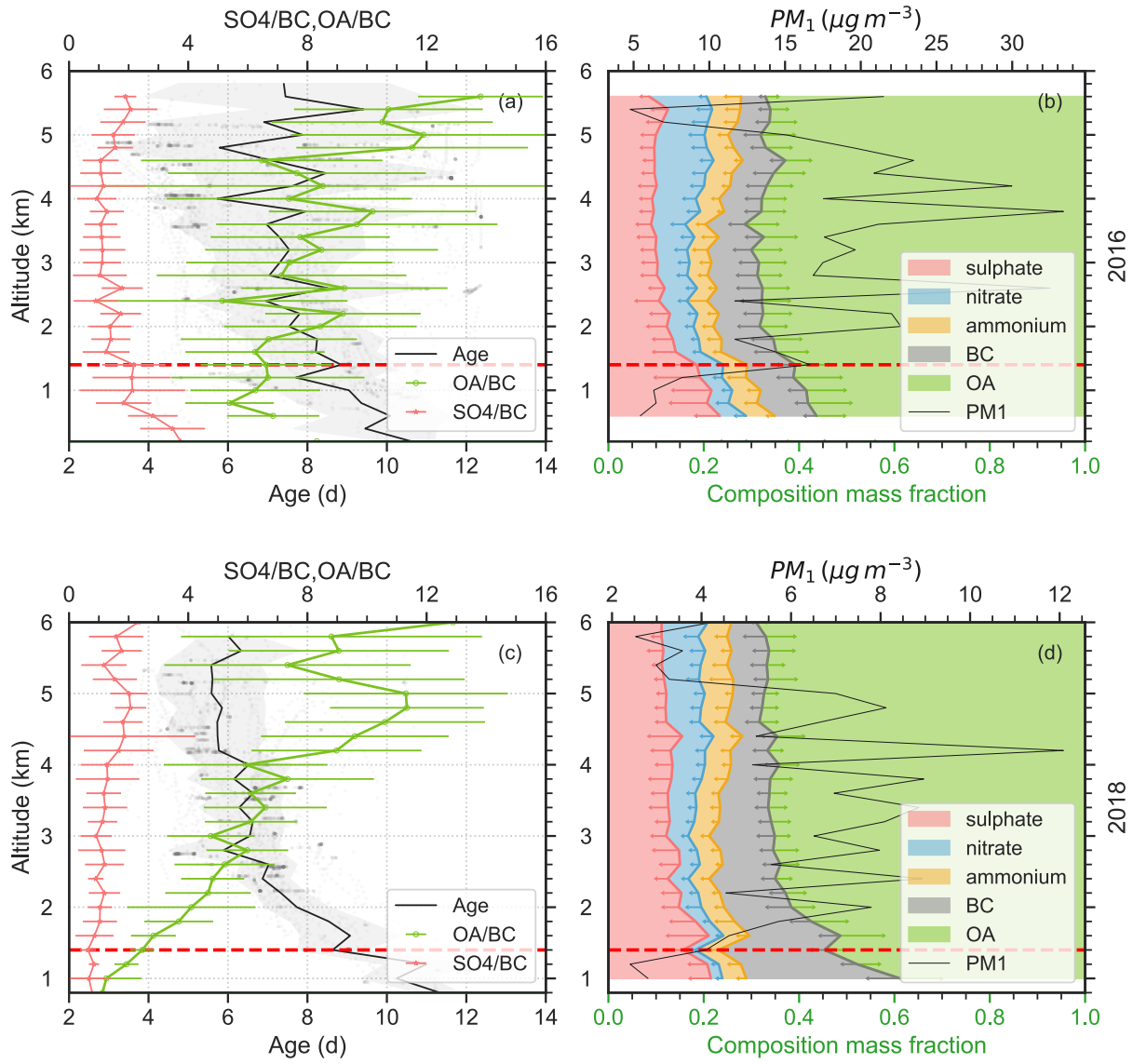

Figure 2. The vertical distribution of plume age and chemical composition. (a, c) Variation of plume age (black), OA/BC, and SO4/BC with altitude in 2016 (upper) and 2018 (lower)

ORACLES campaigns, respectively. Grey dots show the distribution of plume age with the altitude. (b, d) The average vertical distribution of the mass ratio of chemical compositions and the average mass concentration of PM_1 from AMS and SP2 in every 200 m in 2016 and 2018 ORACLES campaigns, respectively. The lines are the mean value in every 200 m bin. Errorbars and grey shading represent the standard deviation in every 200 m bin. The red dashed lines at 1400 m show the maximum height of the MBL during the study period.

Flights in 2016 ORACLES (Fig. 1, yellow lines) are in the region of 8-24° S and 0-15° E, traversing both the southern African Easterly Jet (AEJ-S) region and the continent anticyclone (Ryoo et al., 2021). As a result, aerosols around 3-4 km in 2016 ORACLES include both less aged (<4 d) particles coming directly from the continent and highly aged (>10 d) particles transported from the west/north, resulting in a larger variation of plume age in each level as shown in Fig. 2a. At lower altitudes, aerosols are less aged than those in the 2018 campaign due to the subsidence (positive values of omega) near the Namibian coast (Fig. 1). During the 2016 campaign, the cloud top is generally below 1.5 km. The 2018 ORACLES flights, represented by blue lines in Fig. 1, are primarily situated within the 0-15° S and 5-10° E coordinates. The cloud top in this region is a bit lower than in 2016 campaign, centering around 1 km. This area generally coincides with the region influenced by the southern African Easterly Jet (AEJ-S). BBA are lifted up to the free troposphere, transported westward by AEJ-S and then subside into the marine boundary layer, rendering the distinct vertical age pattern that increases with the decreasing altitude (Fig. 2c). Correspondingly, aerosols in the SEA region during BB season exhibit distinct vertical distribution of chemical composition. From Fig. 2b and 2d, the vertical profiles of chemical composition fractions are generally consistent during 2016 and 2018 ORACLES campaigns. In this section, we focused on the variation of OA and sulphate, two components that dominate aerosol hygroscopicity in the SEA.

OA constitutes the largest fraction of aerosol mass in ORACLES, approximately 60 %. The OA mass fraction in both years shows little variation above 2 km; below this altitude, OA mass fraction decreases with decreasing altitude, in contrast to the trend of the sulphate mass fraction. The OA/BC ratio, representing the OA mass concentration normalised by that of BC to remove the dilution effect during transport and an indication of OA processing, differs in 2016 and 2018. While 2018 data shows a clear decrease in OA/BC with decreasing altitude, the decrease was less pronounced in 2016, showing considerable variation at identical altitudes. In the meanwhile, the OA/BC shows a clear reverse trend with the plume age in 2018, this inverse relationship is less obvious in 2016. Dobracki et al. (2022) used RH as an indicator to investigate the importance of thermodynamic partitioning in OA/BC changes during the 2016 ORACLES campaign, concluding that it accounts for no more than 10 % of the changes. The dominant factor is believed to be the oxidation of OA through fragmentation. A similar result is found in this study using temperature as an indicator, as shown in Fig. 3a. Please note Fig. 3 only considers OA above 1.4 km and temperature > 0 ℃ to minimize the marine influence and to exclude possible ice nucleation. The OA/BC ratio in the 2016 ORACLES campaign did not show a clear decrease with increasing temperature, as NO_3/BC did, which is a result of thermodynamic repartition to the gas phase. However, in the 2018 ORACLES campaign, we did notice a significant decrease of OA/BC with increasing temperature (Fig. 3b). The OA/BC decreased ~70 % from 9.7±3.1 for temperature 0-4 ℃ to 2.9±0.9 for temperature > 20 ℃, only slightly lower than the decrease of NO_3/BC, ~85 %. Yet, we cannot simply attribute the OA/BC changes to thermodynamic repartition while disregarding the effect of ageing or OA oxidation. In 2018, temperature and plume age are closely correlated (Pearson correlation coefficient of 0.51), and the decrease in OA/BC is accompanied by ageing (Pearson correlation coefficient of 0.57), as shown in Fig. 2a and b. We utilized the oxidation state to differentiate between the effects of thermodynamic repartition and OA oxidation. Figure 4 shows the Van Krevelen

diagrams (H/C vs. O/C, Ng et al., 2011) for aerosols at temperatures > 20 ℃ and 0-4 ℃. The estimated carbon oxidation state (OS_C), defined as OS_C=2O/C−H/C, can also indicate different OA volatility regimes, with OSc of -2.0− -1.5 for HOA (hydrocarbon-like OA), -1.75− -0.75 for BBOA (biomass burning OA), -1.0−0.0 for SV-OOA (semi-volatile oxidized OA), and 0.0−1.0 for LV-OOA (low volatility oxidized OA) (Donahue et al., 2012; Kroll et al., 2011). If thermodynamic repartition plays a more crucial role, the OA remaining under higher temperature would be less volatile due to evaporation of more volatile OA. Notably, we found the opposite. From Fig. 4, aerosols at temperature > 20 ℃ (lower altitudes) are generally more volatile than those at temperature 0-4 ℃ (higher altitudes). This indicates that thermodynamic repartition is not a dominant factor in OA/BC changes, and that the OA oxidation through fragmentation is more important in OA/BC changes in 2018, consistent with the 2016 campaign as well as results in Dobracki et al. (2022). This is also in line with the findings of Dang et al. (2022) which found less organics in aerosols collected on filters associated with more aged plumes and more rounded and viscous organics on filters sampled from less aged plumes. For OA below 1.4 km, aqueous phase reactions and cloud scavenging might also contribute to the loss of OA during the entrainment and within the MBL (Che et al., 2022a; Wu et al., 2020).

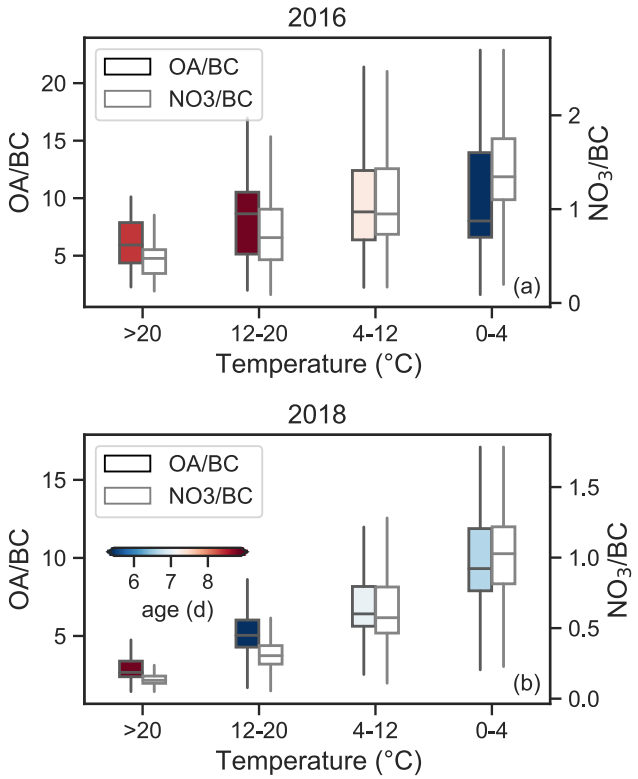

286

287 Figure 3. OA/BC (black outline) and NO_3/BC (grey outline) mass ratios as a function of
288 ambient temperature in 2016 (a) and 2018 (b) ORACLES campaign, for altitude > 1.4 km and
289 temperature > 0 °C. The boxes represent the 10th percentile, 25th percentile, median, 75th
290 percentile, and 90th percentile.

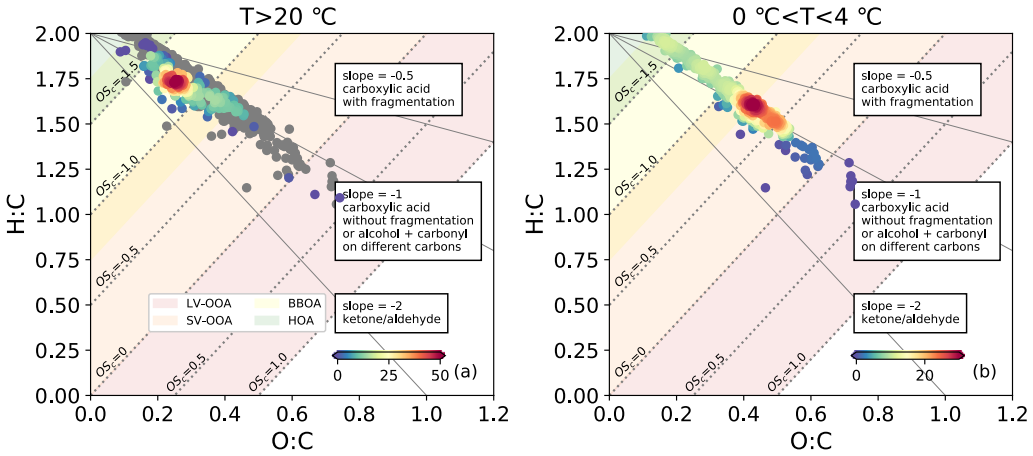

291

292 Figure 4. Van Krevelen diagram (H/C vs. O/C) for aerosols with temperature higher than 20 °C
293 (a) and with temperature lower than 4 °C (b). The color scale indicates the density of the data

294 in each plot. The grey dots in (a) are the Van Krevelen diagram of aerosols with temperature
295 lower than 4 ℃, the same as (b).

296 The variation of sulphate mass fraction remains largely constant above 2 km, and below
297 2 km, increases with decreasing altitudes. The higher sulphate fraction at lower altitudes is
298 consistent with the observations from CLARIFY-2017 (CLoud-Aerosol-Radiation Interaction
299 and Forcing for Year 2017) campaign (Wu et al., 2020), which was conducted downwind of
300 ORACLES in the SEA ocean. This higher sulphate fraction at lower altitudes results from the
301 increase of SO_4/BC and decrease of OA/BC. SO_4/BC ratio generally remains constant above
302 800 m in both years' campaign. However, for 2016 ORACLES campaign, where there are
303 samples below 800 m, the ratio shows an increase with decreasing altitude. This increase could
304 indicate a sulphate contribution from the ocean, either in the form of sea-salt sulphate or
305 through the oxidation of dimethylsulfide (DMS) emitted by marine phytoplankton. The latter
306 can contribute to non-sea-salt sulphate by oxidizing to SO_2 and further to sulphate (Mayer et
307 al., 2020; Alexander et al., 2005). Notably, part of the 2016 flight region, especially the SEA
308 offshore of Namibia, is known as an upwelling region with high DMS emissions (Andreae et
309 al., 1995). Klopper et al. (2020) have attributed 57 % of sulphate to sea salt and 43 % to non-
310 sea-salt sulphate along the Namibian coast. These findings align with model simulations
311 showing that DMS is the third largest CCN source in the SEA up to 2 km (Che et al., 2022b).

312 Furthermore, BC mass constitutes approximately 10 % of the PM_1 mass fraction,
313 indicating the large influence of BB in this region. The nitrate mass fraction increases with
314 increasing altitude in all layers, which is consistent with the findings of CLARIFY, and can be
315 explained by the shift of gas-particle partitioning of the HNO_3-NH_3-NH_4NO_3 system towards
316 the aerosol phase at the lower temperatures found at higher altitudes (Wu et al., 2020). The
317 mass fraction of ammonium stays stable with height, approximately 5 %. We neglected
318 chloride in this study as it accounts for less than 1±1% mass fraction.

3.2 Aerosol hygroscopicity in SEA in 2016 and 2018 ORACLES

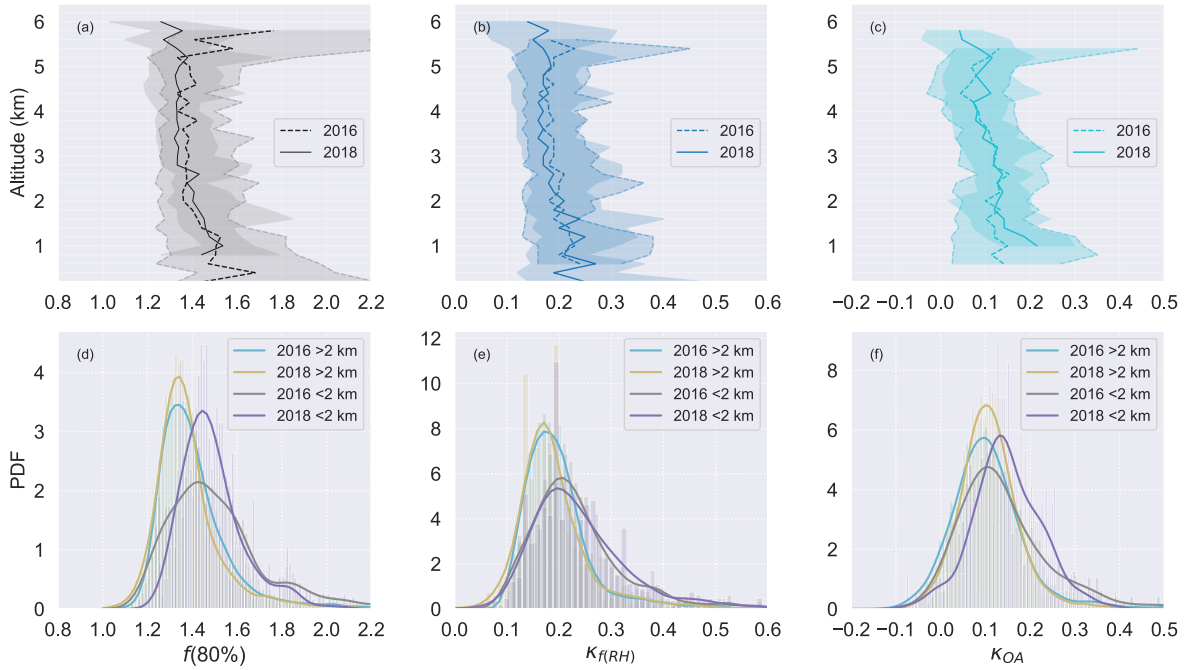

Figure 5. Vertical profiles and PDF of $f(80\%)$ (a, d), $\kappa_{f(RH)}$ (b, e), and κ_{OA} (c, f) for aerosols in the 2016 (dotted line) and 2018 (solid line) ORACLES campaign. The lines in a, b, and c represent the medians, and the shadings in a, b, and c represent the 10th and 90th percentiles.

In general, the aerosol hygroscopicity stays stable above 2 km in both years' campaigns; while below 2 km, aerosols become more hygroscopic at lower altitudes (Fig. 5). The results from the Levene's test for medians for $f(80\%)$, $\kappa_{f(RH)}$, and κ_{OA} indicate that $f(80\%)$, $\kappa_{f(RH)}$, and κ_{OA} are statistically different above and below 2 km, with a confidence level of 95%. This is consistent with the vertical variation of sulphate and OA mass fraction, i.e. more sulphate and less OA at lower altitudes (Fig. S5). The probability density function (PDF) distributions of $f(80\%)$ and $\kappa_{f(RH)}$ are similar in the 2016 and 2018 campaigns, with larger variations and higher values of the aerosol hygroscopicity PDF under 2 km (Fig. 5d and 5e). For $f(80\%)$ below 2 km, a primary mode with a value of around 1.45 is evident, but there is also a second mode with a value of around 1.81 for aerosols in both years. While the second mode is subtle, it can be identified in the PDF of $\kappa_{f(RH)}$ (Fig. 5e). This suggests the presence of highly hygroscopic

substances and could indicate marine influence, as most aerosols below 2 km are within the MBL. For aerosols above 2 km, the mean and standard deviation of $f(80\%)$ and $\kappa_{f(RH)}$ are 1.40±0.17 and 0.19±0.07, respectively (Fig. 5, Table 1, and Table S2). These values indicate less hygroscopic particles (Liu et al., 2011) and are lower than those for marine aerosols (Zieger et al., 2010; Carrico et al., 2003) but higher than those for dust and polluted dust particles (Bukowiecki et al., 2016; Zhang et al., 2015). They are comparable to smoke-dominated aerosols, such as the smoke from savanna fires in Australia (Gras et al., 1999) and the BBA from forest fires in the northeast US (Wang et al., 2007). These values are slightly higher than the $f(80\%)$ in Brazil (SCAR-B) (Kotchenruther and Hobbs, 1998). The particles below 2 km are more hygroscopic (Liu et al., 2011). The mean and standard deviation of $f(80\%)$ and $\kappa_{f(RH)}$ are 1.51±0.22 and 0.23±0.08, respectively, placing them in the upper ranges of BBA hygroscopicity reported in the literature. These values are comparable to those of the aged smoke in Africa (SAFARI, Magi and Hobbs, 2003) and the Yangtze River Delta background station (Zhang et al., 2015). They match the $\kappa_{f(RH)}$ of 0.22 at a rural site in southern China (Kuang et al., 2021) but are lower than the values for BBA in East Asia (ACE-Asia, Kim et al., 2006) and agricultural burning in INDOEX (Indian Ocean Experiment, Sheridan et al., 2002). Comparing to the κ obtained from CCN measurements at a similar location in August 2017 ORACLES (Kacarab et al., 2020), our results are ~ 30 % lower. This difference is expected because κ values obtained under supersaturated conditions are typically larger than those from sub-saturated conditions (Petters and Kreidenweis, 2007). This highlights the significance of using the appropriate κ for sub-saturated and supersaturated investigations, such as when examining aerosol liquid water content and cloud condensation nuclei activation (Rastak et al., 2017; Petters and Kreidenweis, 2007).

Table 1. The $f(RH)$ of biomass burning aerosol from the literature.

$f(RH)$	RH	Location	Fuel type and notes	Reference

1.37	80%	Australia	light-wooded savanna fires	Gras et al., 1999
1.40	82%	northeast US	forest fires	Wang et al., 2007
1.16	80%	Brazil (SCAR-B[a])	grass, shrub, and trees	Kotchenruther and Hobbs, 1998
1.44 ± 0.02	80%	Southern Africa (SAFARI 2000[b])	aged heavy smoke	Magi and Hobbs, 2003
1.60±0.20	85%	Korea (ACE-Asia[c])	BBA	Kim et al., 2006
1.58±0.21	85%	India Ocean (INDOEX[d])	agricultural burning	Sheridan et al., 2002
1.51±0.22	80%	South-East Atlantic Ocean (below 2 km, ORACLES)	savanna[e]	This study
1.40±0.17	80%	South-East Atlantic Ocean (above 2 km, ORACLES)	savanna[e]	This study

[a] Smoke, Clouds, and Radiation-Brazil

[b] Southern African Regional Science Initiative 2000

[c] Aerosol Characterization Experiment

[d] Indian Ocean Experiment

[e] Fuel type discussed in Che et al. (2022c)

The mean κ_{OA} (±1 standard deviation) is 0.11±0.08, with the 25th and 75th percentiles of 0.06 and 0.16. From the vertical profiles, more hygroscopic OA are generally more aged, highly oxidized, and usually located at lower altitudes (Fig. 2 and 5). In addition, we observed a slight increase in κ_{OA} with volatility in 2016, with a Pearson correlation coefficient of -0.35 between κ_{OA} and OSc, contrasting the conventional understanding that the most volatile compounds have the least hygroscopicity. This trend has been observed, albeit rarely, in field and laboratory studies (e.g. Cerully et al., 2015; AsaAwuku et al., 2009). It may be related to fragmentation during OA oxidation, where the highly aged and low volatile OA may dissociate into more volatile fragments that are still highly functionalized and hygroscopic. However, in general, no clear correlation has been found between κ_{OA} with altitude or oxidation level.

We noted a portion of highly aged aerosols (> 10 d) in 2016 having high OA/BC (> 12, corresponding OA mass fraction > 50 %), in contrast to the general trend that more aged aerosols correspond to smaller OA/BC (Fig. 2). About 95 % of these aerosols are above 3 km and have a slightly lower f_{44} than the campaign average (Fig. S6a). Approximately 60 % belong to LV-OOA with OSc > 0 and 40 % are SV-OOA (Fig. S6b). As shown in Fig. S6c, the κ_{OA} values are smaller for these aerosols compared to the whole 2016 campaign, which is consistent with previous studies that κ_{OA} is lower for less oxidized OA (Kuang et al., 2020a; Rastak et al., 2017; Mei et al., 2013); though we do not observe such correlation for the entire campaign. We hypothesize that thermodynamic repartitioning has played a role, i.e. less-oxidized materials condensed onto pre-existing OA under low temperature at high altitudes, resulting in smaller f_{44} values and contributing to SV-OOA. These less-oxidized materials are generally less functionalized and less hygroscopic, which would lead to a lower κ_{OA}.

3.3 Relationship with chemical composition and κ_{OA}

3.3.1 Comparison with various campaigns

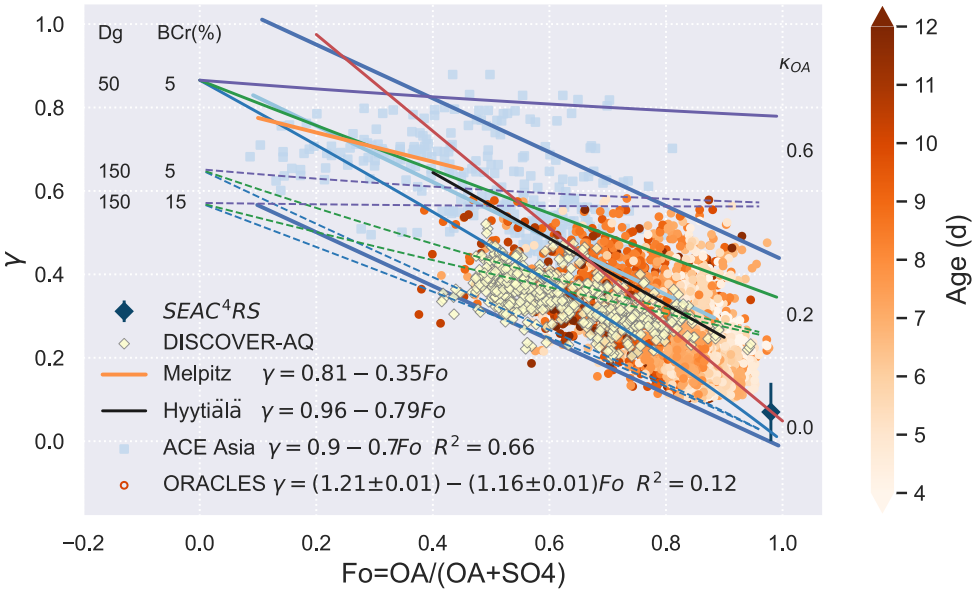

Figure 6. γ versus Fo in various campaigns and for internally mixed OA-$(NH_4)_2SO_4$-BC mixtures. Fo represents the ratio of mass concentrations of OA to OA and SO_4^{2-}. Solid lines in light blue and red represent the linear fits for ACE-Asia and ORACLES, respectively. Solid blue lines show the 95% prediction bands for the ACE-Asia data, in light blue rectangles, taken from Quinn et al. (2005). Colorbar represents the plume age (days) in ORACLES. Data for SEAC^{4}RS is shown by dark blue diamond, taken from Shingler et al. (2016). DISCOVER-AQ data is shown by yellow diamonds, taken from NASA Langley Research Center Atmospheric Science Data Center (Atmospheric Science Data Center, 2015). Fitting lines for two European sites Melpitz (solid orange line) and Hyytiälä (solid black line) are from Zieger et al. (2015). Blue, green, and purple lines represent results for internally mixed OA-$(NH_4)_2SO_4$-BC mixtures with 1) a range of BC mass fraction (BCr, solid for 5% and dashed for 25%) and 2) OA with κ_{OA} of 0 (blue), 0.2 (green), and 0.6 (purple) from Mie calculations assuming a lognormal size distribution with a geometric mean diameter D_{gn} of 150 nm and a standard deviation σ_{sg} of 1.6.

Quinn et al. (2005) proposed a parameterization quantifying the relationship between γ and Fo, the ratio of mass concentrations of OA to OA and SO_4^{2-}, based on measurements in ACE-Asia. We applied the parameterization to ORACLES measurements and as shown in Fig. 6, our data are well within the 95% prediction confidence intervals. We further investigated the γ-Fo dependence of BBA from DISCOVER-AQ and SEAC^{4}RS (Shingler et al., 2016) and continental aerosols from the central European station Melpitz and a boreal site Hyytiälä in Finland (Zieger et al., 2014, 2015), all showed good overlap with those from ACE-Asia and ORACLES. The linear regression for ORACLES, $\gamma = (1.16\pm0.02) - (1.11\pm0.02)\cdot Fo$, retrieved from an orthogonal fit by taking the standard deviation as the input for uncertainty calculation, is very similar to those in Hyytiälä and ACE-Asia, though the slope is slightly lower.

We explored the γ-Fo relationship with the Mie model and found that the relationship observed can be largely explained by aerosol chemical composition and OA hygroscopicity. The γ values were calculated with the scattering coefficients simulated at both dry conditions and 80 % RH were performed with Mie model for internally mixed OA-$(NH_4)_2SO_4$-BC mixtures with assumed BC mass ratio (BCr, 5 % and 25 %), and κ_{OA} values (0-0.6), which encompass the ranges observed in ORACLES (refer to Sect. 3.2 for κ_{OA} values). The PNSD was assumed to be lognormally distributed, with the geometric mean diameter (D_{gn}) of 150 nm and the standard deviation (σ_{sg}) of 1.6. As shown in Fig. 6 (solid and dashed purple, green, and blue lines), simulated curves can capture most of the observations. Fo and κ_{OA} dominant γ, and BC shows a small negative impact. It is noteworthy that the (negative) slope of the γ-Fo relationship increases with increasing κ_{OA} up to κ_{OA} values of 0.6, where γ exhibits little variation with Fo. Therefore, we conclude that the variation of BBA hygroscopicity with ageing in the SEA is mainly due to changes in chemical composition, particularly sulphate and OA, as well as the variation of OA hygroscopicity during transport. The higher BC fraction in aged aerosols compared to less aged ones has slightly decreased the hygroscopicity of aged aerosols.

3.3.2 Parameterization of γ using Mie simulations of internally mixed OA-$(NH_4)_2SO_4$-BC mixtures

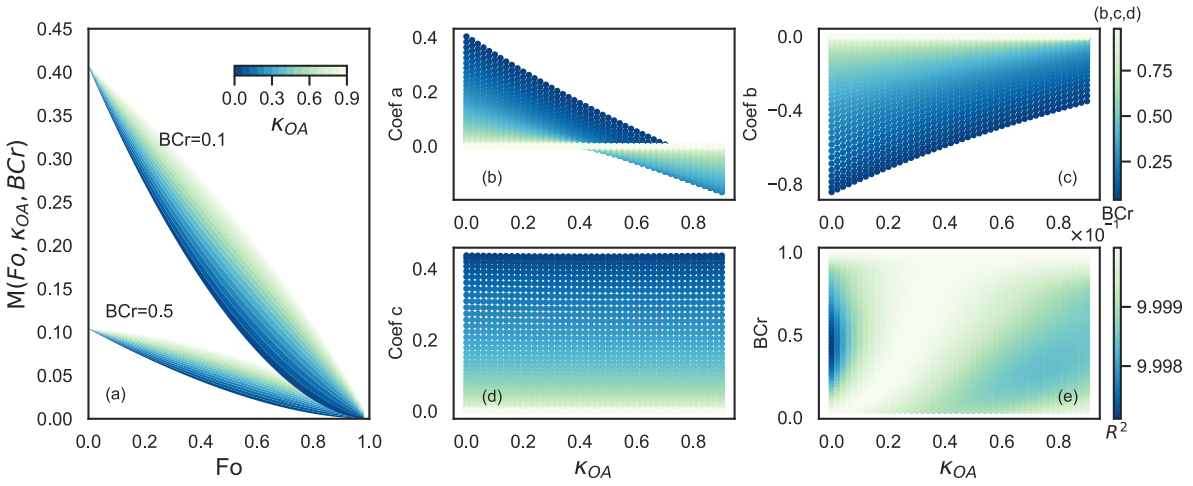

Figure 7. (a) Variations of M(Fo,κ_{OA},BCr) with Fo coloured by κ_{OA} at BCr of 0.1 and 0.5, respectively, for internally mixed OA-$(NH_4)_2SO_4$-BC mixtures. M(Fo,κ_{OA},BCr) is the product of γ(Fo,κ_{OA}=0,BCr) and γ(Fo,κ_{OA},BCr) for each κ_{OA} value. Fo represents the ratio of the mass concentration of OA to that of OA and SO_4^{2-}. BCr is the mass ratio of BC. (b,c,d) Variation of coefficients a, b, and c with κ_{OA} and BCr. The coefficients a, b, and c are the fitted parameters of the quadratic regression between M(Fo,κ_{OA},BCr) and Fo for each κ_{OA} and BCr. (e) The R^2 (colorbar) of the M(Fo,κ_{OA},BCr) regression with Fo as a function of κ_{OA} and BCr.

Mie simulations are performed for internally mixed OA-$(NH_4)_2SO_4$-BC mixtures to obtain the scattering coefficient of dry and humidified aerosols. We assume PNSD to be a log-normal distribution with D_{gn}=150 nm and σ_{sg} = 1.6, as the approximation of the D_{gn} and σ_{sg} in ORACLES 2016 and 2018 campaigns. The RH and RH_{ref} is set as 80 % and 0, respectively. The γ is then calculated following Eq. 2. The Fo, κ_{OA}, and BCr are varied from 0 to 1, 0 to 0.9, and 0 to 1, respectively, all in increments of 0.02. Taking γ(Fo,κ_{OA}=0,BCr) as the baseline (refer to solid and dashed blue lines in Fig. 6), we calculated the product M(Fo,κ_{OA},BCr) of γ(Fo,κ_{OA}=0,BCr) and γ(Fo,κ_{OA},BCr) for each κ_{OA} and BCr, i.e. M(Fo,κ_{OA},BCr)= γ(Fo,κ_{OA}=0,BCr)* γ(Fo,κ_{OA},BCr), and found that the relationship between M(Fo,κ_{OA},BCr) and Fo can be well fitted into a quadratic (second-order) polynomial function, i.e. M(Fo,κ_{OA},BCr) = $aFo^2+bFo+c$ (Fig. 7a). The variation of M(Fo,κ_{OA},BCr) with Fo and the R^2 of the regression are shown in Fig. 7a and 7e, respectively. The fitted coefficients a, b, and c, as shown in Fig. 7b, 7c, and 7d, coincidentally fit well as quadratic functions of κ_{OA}, whose coefficients, in turn, can be well fitted into a fifth-order polynomial function of BCr. Results are shown in Fig. S3 in the supplement. In sum, the M(Fo,κ_{OA},BCr) can be parameterized as:

$$\boldsymbol{M(F_o, \kappa_{OA}, BCr) = \sum_{\substack{i\le 2\\ j\le 2\\ k\le 5}} a_{ijk} BCr^k \kappa_{OA}^j F_o^i} \quad (4)$$

Similarly, $\gamma(Fo,\kappa_{OA}=0,BCr)$ can be well fitted into a quadratic function of Fo with coefficients that fit well with a fifth-order polynomial function of BCr:

$$\boldsymbol{\gamma(F_o, \kappa_{OA} = 0, BCr) = \sum_{\substack{i\leq 2 \\ k\leq 5}} a_{ik} BCr^k F_o^i} \quad (5)$$

Equations 4 and 5 in matrix format are referred to Eq. S1 and S2 in the supplement, respectively. Values of coefficients a_{ijk} and a_{ik} are shown in Table S3. Therefore, $\gamma(Fo,\kappa_{OA},BCr)$ can be calculated as the ratio of $M(Fo,\kappa_{OA},BCr)$ to $\gamma(Fo,\kappa_{OA}=0,BCr)$:

$$\boldsymbol{\gamma(Fo, \kappa_{OA}, BCr) = M(F_o, \kappa_{OA}, BCr)/\gamma(F_o, \kappa_{OA} = 0, BCr)} \quad (6)$$

We evaluated this parameterization by comparing the predicted and measured $f(80\%)$ in ORACLES 2016 and 2018 campaigns. The predicted $f(80\%)$ is calculated with Eq. 6 with Fo, κ_{OA}, and BCr as inputs and Eq. 2 with the dry and humidified RHs measured in both campaigns. Note the mean BC mass ratio for each year has been used in the calculation, as little difference has been observed using the temporal BCr and mean BCr. Good correlation of measured and predicted $f(80\%)$ has been achieved for both years' campaign, as shown in Fig. 8a. This indicates that the internally mixed OA-$(NH_4)_2SO_4$-BC mixture with PNSD (D_{gn}=150 nm and σ_{sg} = 1.6) is a good approximation of aerosols with respect to the $f(RH)$ prediction in 2016 and 2018 ORACLES campaign. The influence of PNSD on $f(RH)$ is small and discussed in Section S1 in the supplement.

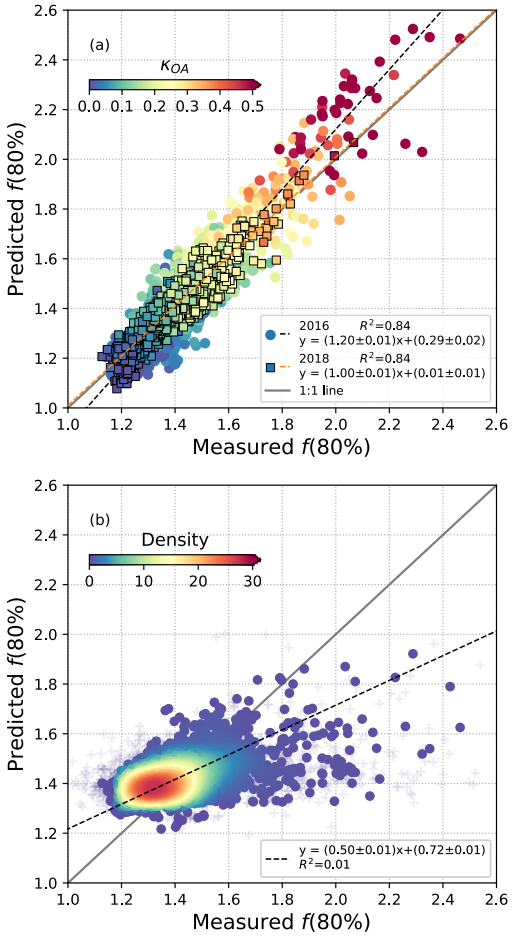

Figure 8. Measured f(80%) vs predicted f(80%) using the γ parameterization for internally mixed OA-$(NH_4)_2SO_4$-BC mixtures. The f(80%) in subplot (a) is calculated with κ_{OA} values coloured by κ_{OA}, and in subplot (b) is predicted with the mean κ_{OA} values. Black and orange dashed lines in subplot (a) represent the ordinary linear regression for 2016 and 2018, respectively. The black dashed line in subplot (b) represents the ordinary linear regression for the two years. Grey solid line is the 1:1 line.

3.3.3 Sensitivity of aerosol scattering enhancement to κ_{OA}

Due to the chemical complexity of OA, the κ_{OA} values of particles are not easily obtained. Various hygroscopicity parameterizations have been proposed in previous studies, most of which are parameterized with chemical composition, e.g. organics or inorganics fraction, and a constant assumed κ_{OA} value. Few studies consider the variation of κ_{OA} (Zhang

et al., 2015; Huang et al., 2022). While these parameterizations can represent their observations well, they may not be suitable for situations with different κ_{OA} values. Therefore, in this section, the influence of κ_{OA} on the prediction of f(RH) is analyzed. We calculated the f(80%) with the mean κ_{OA} in each campaign and the results are shown in Fig. 8b. The use of a constant κ_{OA} average leads to a much smaller variation of the predicted f(80%) values, with most of which concentrated around 1.3-1.4. Predicted f(80%) tend to overestimate lower f(80%) values while underestimate higher f(80%) values. A slope of 0.50 and a R^2 of 0.01 indicates poor prediction in capturing the trend of f(80%). This indicates that using Fo, BCr, and a constant κ_{OA} is insufficient for the prediction of f(RH), and that the variation of κ_{OA} need to be considered, at least for situations where κ_{OA} has a large variation, such as in ORACLES.

To quantitatively investigate the sensitivity of f(RH) to κ_{OA}, we calculated the deviation of f(80%) with κ_{OA} for the OA-$(NH_4)_2SO_4$-BC mixture. The deviation of f(80%) was calculated as f(80%, κ_{OA})-f(80%, κ_{OA}=0). As shown in Fig. 9, we observed that κ_{OA} is positively correlated with f(80%). Additionally, the deviation of f(80%) is dependent on the OA fraction (Fo), i.e. a higher OA fraction leads to a larger impact of κ_{OA} and consequently a larger deviation of f(80%).

The 25th and 75th percentiles of Fo in 2016 and 2018 ORACLES campaign were 0.74 and 0.86, respectively. These are relatively high values and therefore result in relatively high spread of f(80%). Additionally, the age of ORACLES OA spans from <4 days to > 10 days, during which OA oxidation and fragmentation (as discussed in Section 3.2) takes place. These processes alter the hygroscopicity of OA, causing the OA in ORACLES to contribute to large variations of κ_{OA}. These large variations of κ_{OA}, combined with the relatively high OA fraction (Fo), makes f(RH) highly sensitive to the κ_{OA} value. For aerosols with a κ_{OA} of 0.4 and a Fo of 0.86, the f(80%) can be 80 % higher compared to aerosols with hydrophobic OA, as shown in Fig. 9. In other words, the aerosol scattering coefficients at 80 % RH are 80 % higher solely

because of the increase of OA hygroscopicity. This high sensitivity also explains the poor prediction of f(80%) when using campaign mean κ_{OA} values, as shown in Fig. 8b. Many studies overlook the variability of κ_{OA} and instead use a constant κ_{OA} when analyzing aerosol hygroscopicity or radiative forcing. As illustrated in Fig. 9, this can be reasonable when the OA fraction is low and κ_{OA} exhibits minimal variation; however, in cases where these two conditions are not met, κ_{OA} can significantly influence the scattering coefficients and hence direct radiative forcing.

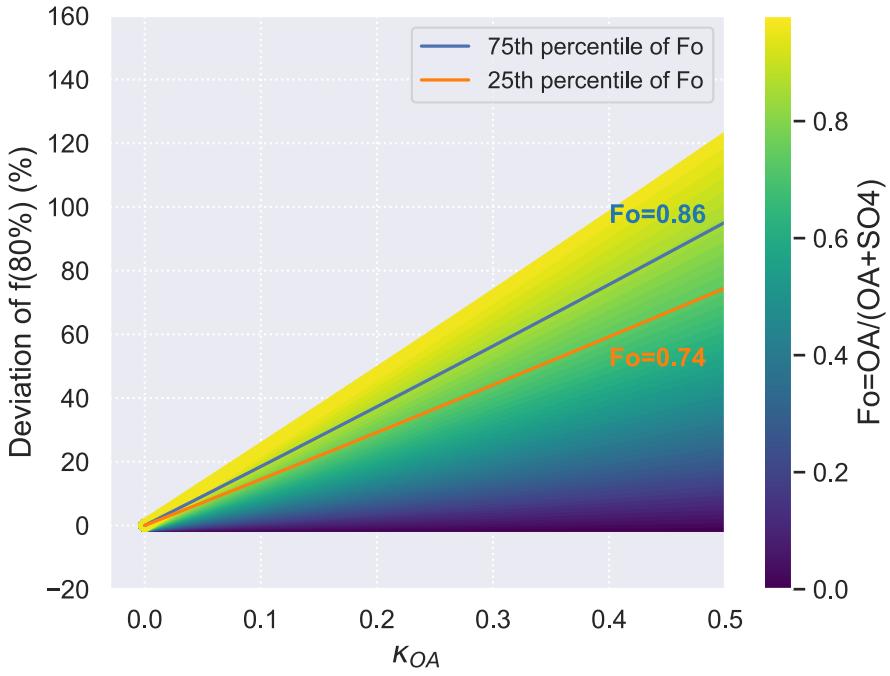

Figure 9. Sensitivity of the deviation of f(80%) to κ_{OA}. The deviation of f(80%) was calculated as f(80%, κ_{OA})-f(80%, κ_{OA}=0). The OA to OA + SO_4 ratio (Fo) is represented by the colorbar. The blue and orange lines represent the variation at 75th and 25th percentile of Fo in both years' ORACLES campaign, respectively.

4 Conclusion

The hygroscopicity of aerosols from the perspective of scattering enhancement over the SEA Ocean during the BB season are investigated using measurements from the 2016 and 2018

ORACLES campaigns. The vertical distribution of aerosol hygroscopicity shows a consistent pattern in both campaigns, remaining stable above 2 km; below 2 km, aerosols are more hygroscopic at lower altitudes. Aerosols above 2 km have a mean and standard deviation of $f(80\%)$ and $\kappa_{f(RH)}$ of 1.40±0.17 and 0.19±0.07, respectively, and are less hygroscopic. Conversely, aerosols below 2 km are more hygroscopic, and have a mean and standard deviation of $f(80\%)$ and $\kappa_{f(RH)}$ of 1.51±0.22 and 0.23±0.08, respectively, which are values at the upper level of BBA hygroscopicity found in the literature. This variation of aerosol hygroscopicity is consistent with the vertical variation of chemical composition. The OA and sulphate mass fraction in both years show little variation above 2 km; while below this altitude, OA decreases with decreasing altitude, while the sulphate mass fraction tends to increase. OA oxidation through molecular fragmentation is the main mechanism for OA losses in the FT. While the increase of sulphate in the MBL could indicate marine influence.

We retrieved κ_{OA} using Mie simulations. It shows a large variation, with the mean and standard deviation being 0.11±0.08 and the 25^{th} and 75^{th} percentiles of 0.06 and 0.16, respectively. No clear relationship was found between κ_{OA} and OA oxidation level; while a slight increase in κ_{OA} with volatility is shown in 2016, which may be related to the fragmentation during OA oxidation, where the highly aged and low volatile OA may dissociate into more volatile fragments that are still highly functionalized and hygroscopic. In all, OA hygroscopicity under sub-saturated conditions can be largely influenced by solubility, molecular weight, molecular functional groups, and carbon number (Cai et al., 2021; Kuang et al., 2020a; Rastak et al., 2017; Rickards et al., 2013; Suda et al., 2012); to better understand the variation of κ_{OA}, more molecular investigations are needed.

In comparison with other campaigns, we find the variation of aerosol hygroscopicity in the SEA is mainly due to changes in chemical composition, particularly sulphate and OA, as well as variations in OA hygroscopicity during transport. To quantitatively investigate this

546 relationship, we came up with a parameterization using Fo, BCr, and κ_{OA}, and the f(80%) from
547 Mie simulations for internally mixed OA-$(NH_4)_2SO_4$-BC mixture with PNSD (D_{gn}=150 nm
548 and σ_{sg}=1.6). This suggests that the internal mixture of OA-$(NH_4)_2SO_4$-BC is a good
549 approximation of aerosols with respect to the f(RH) prediction in 2016 and 2018 ORACLES
550 campaign.

551 A sensitivity study indicates that solely due to the increase in OA hygroscopicity
552 observed in our study, the aerosol scattering coefficients at 80 % RH can be amplified by 80 %.
553 Relying on the campaign's mean κ_{OA} value leads to a poor prediction of f(80%). The
554 dependence of f(RH) on κ_{OA} suggests that using a constant κ_{OA} can be acceptable when the OA
555 fraction is low and κ_{OA} demonstrates limited variations. However, in situations where these
556 two conditions are not met, κ_{OA} can significantly influence the scattering coefficients and thus
557 aerosol radiative effect. Therefore, accommodating the variability of κ_{OA} is advisable.

558

559 *Competing interests.* At least one of the (co-)authors is a guest member of the editorial board
560 of Atmospheric Chemistry and Physics for the special issue "New observations and related
561 modelling studies of the aerosol-cloud-climate system in the Southeast Atlantic and southern
562 Africa regions". The authors have no other competing interests to declare.

563

564 *Special issue statement.* This article is part of the special issue "New observations and related
565 modeling studies of the aerosol-cloud-climate system in the Southeast Atlantic and southern
566 Africa regions (ACP/AMT inter-journal SI)". It is not associated with a conference.

567

568 *Data Availability.* Data sets are publicly available via the digital object identifier provided
569 under ORACLES Science Team reference:
570 https://doi.org/10.5067/Suborbital/ORACLES/P3/2018_V2.

Acknowledgments. The authors would like to thank the ORACLES team. Lu Zhang thanks the postdoctoral fellowship funding from Tel Aviv University, Department of Exact Sciences. Michal Segal-Rozenhaimer and Haochi Che were supported by United States Department of Energy Atmospheric System Research (ASR) grant DE-SC0020084. Caroline Dang thanks the NASA Postdoctoral Fellowship Grant. Paola Formenti is supported by the AErosols, RadiatiOn and CLOuds in southern Africa (AEROCLO-sA) project funded by the French National Research Agency under grant agreement n° ANR-15-CE01-0014-01, the French national programs LEFE/INSU and PNTS, the French National Agency for Space Studies (CNES), the European Union's 7th Framework Programme (FP7/2014-2018) under EUFAR2 contract n°312609, and the South African National Research Foundation (NRF) under grant UID 105958. The authors thank Paul Zieger for useful comments on this article.

Financial support. This research has been supported by the Tel Aviv University (postdoctoral fellowship); the United States Department of Energy (DOE) Atmospheric System Research (ASR; grant DE-SC0020084); a NASA postdoctoral fellowship; the AErosols, RadiatiOn and CLOuds in southern Africa (AEROCLO-sA) project funded by the French National Research Agency (grant agreement no. ANR-15-CE01-0014-01); the French national programs LEFE/INSU and PNTS; the French National Agency for Space Studies (CNES); the European Union's Seventh Framework Programme (FP7/2014-2018; EUFAR2 contract no. 312609); and the South African National Research Foundation (NRF; grant UID 105958).

References

595 Alexander, B., Park, R. J., Jacob, D. J., Li, Q. B., Yantosca, R. M., Savarino, J., Lee, C. C.
596 W., and Thiemens, M. H.: Sulfate formation in sea-salt aerosols: Constraints from oxygen
597 isotopes, J. Geophys. Res. Atmospheres, 110, https://doi.org/10.1029/2004JD005659, 2005.

598 Andreae, M. O., Elbert, W., and de Mora, S. J.: Biogenic sulfur emissions and aerosols over
599 the tropical South Atlantic: 3. Atmospheric dimethylsulfide, aerosols and cloud condensation
600 nuclei, J. Geophys. Res. Atmospheres, 100, 11335–11356,
601 https://doi.org/10.1029/94JD02828, 1995.

602 Bukowiecki, N., Weingartner, E., Gysel, M., Coen, M. C., Zieger, P., Herrmann, E.,
603 Steinbacher, M., Ga¨ggeler, H. W., and Baltensperger, U.: A Review of More than 20 Years
604 of Aerosol Observation at the High Altitude Research Station Jungfraujoch, Switzerland
605 (3580 m asl), Aerosol Air Qual. Res., 16, 764–788,
606 https://doi.org/10.4209/aaqr.2015.05.0305, 2016.

607 Burgos, M. A., Andrews, E., Titos, G., Benedetti, A., Bian, H., Buchard, V., Curci, G.,
608 Kipling, Z., Kirkevåg, A., Kokkola, H., Laakso, A., Letertre-Danczak, J., Lund, M. T.,
609 Matsui, H., Myhre, G., Randles, C., Schulz, M., van Noije, T., Zhang, K., Alados-Arboledas,
610 L., Baltensperger, U., Jefferson, A., Sherman, J., Sun, J., Weingartner, E., and Zieger, P.: A
611 global model–measurement evaluation of particle light scattering coefficients at elevated
612 relative humidity, Atmospheric Chem. Phys., 20, 10231–10258, https://doi.org/10.5194/acp-
613 20-10231-2020, 2020.

614 Cai, M., Liang, B., Sun, Q., Liu, L., Yuan, B., Shao, M., Huang, S., Peng, Y., Wang, Z., Tan,
615 H., Li, F., Xu, H., Chen, D., and Zhao, J.: The important roles of surface tension and growth
616 rate in the contribution of new particle formation (NPF) to cloud condensation nuclei (CCN)
617 number concentration: evidence from field measurements in southern China, Atmospheric
618 Chem. Phys., 21, 8575–8592, https://doi.org/10.5194/acp-21-8575-2021, 2021.

619 Carrico, C. M., Kus, P., Rood, M. J., Quinn, P. K., and Bates, T. S.: Mixtures of pollution,
620 dust, sea salt, and volcanic aerosol during ACE-Asia: Radiative properties as a function of
621 relative humidity, J. Geophys. Res. Atmospheres, 108,
622 https://doi.org/10.1029/2003JD003405, 2003.

623 Cerully, K. M., Bougiatioti, A., Hite, J. R. J., Guo, H., Xu, L., Ng, N. L., Weber, R., and
624 Nenes, A.: On the link between hygroscopicity, volatility, and oxidation state of ambient and
625 water-soluble aerosols in the southeastern United States, Atmospheric Chem. Phys., 15,
626 8679–8694, https://doi.org/10.5194/acp-15-8679-2015, 2015.

627 Che, H., Zhang, X., Zhang, L., Wang, Y., Zhang, Y., Shen, X., Ma, Q., Sun, J., and Zhong, J.:
628 Prediction of size-resolved number concentration of cloud condensation nuclei and long-term
629 measurements of their activation characteristics, Sci. Rep., 7, 5819,
630 https://doi.org/10.1038/s41598-017-05998-3, 2017.

631 Che, H., Segal-Rozenhaimer, M., Zhang, L., Dang, C., Zuidema, P., Dobracki, A., Sedlacek,
632 A. J., Coe, H., Wu, H., Taylor, J., Zhang, X., Redemann, J., and Haywood, J.: Cloud
633 processing and weeklong ageing affect biomass burning aerosol properties over the south-
634 eastern Atlantic, Commun. Earth Environ., 3, 182, https://doi.org/10.1038/s43247-022-
635 00517-3, 2022a.

Che, H., Stier, P., Watson-Parris, D., Gordon, H., and Deaconu, L.: Source attribution of cloud condensation nuclei and their impact on stratocumulus clouds and radiation in the south-eastern Atlantic, Atmospheric Chem. Phys., 22, 10789–10807, https://doi.org/10.5194/acp-22-10789-2022, 2022b.

Che, H., Segal-Rozenhaimer, M., Zhang, L., Dang, C., Zuidema, P., Sedlacek III, A. J., Zhang, X., and Flynn, C.: Seasonal variations in fire conditions are important drivers in the trend of aerosol optical properties over the south-eastern Atlantic, Atmospheric Chemistry and Physics, 22, 8767–8785, https://doi.org/10.5194/acp-22-8767-2022, 2022c.

Chen, J., Zhao, C. S., Ma, N., and Yan, P.: Aerosol hygroscopicity parameter derived from the light scattering enhancement factor measurements in the North China Plain, Atmospheric Chem. Phys., 14, 8105–8118, https://doi.org/10.5194/acp-14-8105-2014, 2014.

Cotterell, M. I., Willoughby, R. E., Bzdek, B. R., Orr-Ewing, A. J., and Reid, J. P.: A complete parameterisation of the relative humidity and wavelength dependence of the refractive index of hygroscopic inorganic aerosol particles, Atmospheric Chem. Phys., 17, 9837–9851, https://doi.org/10.5194/acp-17-9837-2017, 2017.

Covert, D. S., Charlson, R. J., and Ahlquist, N. C.: A Study of the Relationship of Chemical Composition and Humidity to Light Scattering by Aerosols, J. Appl. Meteorol., 11, 968–976, https://doi.org/10.1175/1520-0450(1972)011<0968:ASOTRO>2.0.CO;2, 1972.

Cubison, M. J., Ortega, A. M., Hayes, P. L., Farmer, D. K., Day, D., Lechner, M. J., Brune, W. H., Apel, E., Diskin, G. S., Fisher, J. A., Fuelberg, H. E., Hecobian, A., Knapp, D. J., Mikoviny, T., Riemer, D., Sachse, G. W., Sessions, W., Weber, R. J., Weinheimer, A. J., Wisthaler, A., and Jimenez, J. L.: Effects of aging on organic aerosol from open biomass burning smoke in aircraft and laboratory studies, Atmospheric Chem. Phys., 11, 12049–12064, https://doi.org/10.5194/acp-11-12049-2011, 2011.

Day, D. E., Hand, J. L., Carrico, C. M., Engling, G., and Malm, W. C.: Humidification factors from laboratory studies of fresh smoke from biomass fuels, J. Geophys. Res. Atmospheres, 111, https://doi.org/10.1029/2006JD007221, 2006.

DeCarlo, P. F., Slowik, J. G., Worsnop, D. R., Davidovits, P., and Jimenez, J. L.: Particle Morphology and Density Characterization by Combined Mobility and Aerodynamic Diameter Measurements. Part 1: Theory, Aerosol Sci. Technol., 38, 1185–1205, https://doi.org/10.1080/027868290903907, 2004.

Ervens, B., Cubison, M., Andrews, E., Feingold, G., Ogren, J. A., Jimenez, J. L., DeCarlo, P., and Nenes, A.: Prediction of cloud condensation nucleus number concentration using measurements of aerosol size distributions and composition and light scattering enhancement due to humidity, J. Geophys. Res. Atmospheres, 112, https://doi.org/10.1029/2006JD007426, 2007.

Gras, J. L., Jensen, J. B., Okada, K., Ikegami, M., Zaizen, Y., and Makino, Y.: Some optical properties of smoke aerosol in Indonesia and tropical Australia, Geophys. Res. Lett., 26, 1393–1396, https://doi.org/10.1029/1999GL900275, 1999.

Gysel, M., Crosier, J., Topping, D. O., Whitehead, J. D., Bower, K. N., Cubison, M. J., Williams, P. I., Flynn, M. J., McFiggans, G. B., and Coe, H.: Closure study between chemical

composition and hygroscopic growth of aerosol particles during TORCH2, Atmospheric Chem. Phys., 7, 6131–6144, https://doi.org/10.5194/acp-7-6131-2007, 2007.

Haywood, J., Bush, M., Abel, S., Claxton, B., Coe, H., Crosier, J., Harrison, M., Macpherson, B., Naylor, M., and Osborne, S.: Prediction of visibility and aerosol within the operational Met Office Unified Model. II: Validation of model performance using observational data, Q. J. R. Meteorol. Soc., 134, 1817–1832, https://doi.org/10.1002/qj.275, 2008.

Howell, S. G., Freitag, S., Dobracki, A., Smirnow, N., and Sedlacek III, A. J.: Undersizing of aged African biomass burning aerosol by an ultra-high-sensitivity aerosol spectrometer, Atmospheric Meas. Tech., 14, 7381–7404, https://doi.org/10.5194/amt-14-7381-2021, 2021.

Huang, S., Wu, Z., Wang, Y., Poulain, L., Höpner, F., Merkel, M., Herrmann, H., and Wiedensohler, A.: Aerosol Hygroscopicity and its Link to Chemical Composition in a Remote Marine Environment Based on Three Transatlantic Measurements, Environ. Sci. Technol., https://doi.org/10.1021/acs.est.2c00785, 2022.

Kacarab, M., Thornhill, K. L., Dobracki, A., Howell, S. G., O'Brien, J. R., Freitag, S., Poellot, M. R., Wood, R., Zuidema, P., Redemann, J., and Nenes, A.: Biomass burning aerosol as a modulator of the droplet number in the southeast Atlantic region, Atmospheric Chem. Phys., 20, 3029–3040, https://doi.org/10.5194/acp-20-3029-2020, 2020.

Kim, J., Yoon, S.-C., Jefferson, A., and Kim, S.-W.: Aerosol hygroscopic properties during Asian dust, pollution, and biomass burning episodes at Gosan, Korea in April 2001, Atmos. Environ., 40, 1550–1560, https://doi.org/10.1016/j.atmosenv.2005.10.044, 2006.

Klopper, D., Formenti, P., Namwoonde, A., Cazaunau, M., Chevaillier, S., Feron, A., Gaimoz, C., Hease, P., Lahmidi, F., Mirande-Bret, C., Triquet, S., Zeng, Z., and Piketh, S. J.: Chemical composition and source apportionment of atmospheric aerosols on the Namibian coast, Atmospheric Chem. Phys., 20, 15811–15833, https://doi.org/10.5194/acp-20-15811-2020, 2020.

Kotchenruther, R. A. and Hobbs, P. V.: Humidification factors of aerosols from biomass burning in Brazil, J. Geophys. Res. Atmospheres, 103, 32081–32089, https://doi.org/10.1029/98JD00340, 1998.

Kuang, Y., Xu, W., Tao, J., Ma, N., Zhao, C., and Shao, M.: A Review on Laboratory Studies and Field Measurements of Atmospheric Organic Aerosol Hygroscopicity and Its Parameterization Based on Oxidation Levels, Curr. Pollut. Rep., 6, 410–424, https://doi.org/10.1007/s40726-020-00164-2, 2020a.

Kuang, Y., He, Y., Xu, W., Zhao, P., Cheng, Y., Zhao, G., Tao, J., Ma, N., Su, H., Zhang, Y., Sun, J., Cheng, P., Yang, W., Zhang, S., Wu, C., Sun, Y., and Zhao, C.: Distinct diurnal variation in organic aerosol hygroscopicity and its relationship with oxygenated organic aerosol, Atmospheric Chemistry and Physics, 20, 865–880, https://doi.org/10.5194/acp-20-865-2020, 2020b.

Kuang, Y., Huang, S., Xue, B., Luo, B., Song, Q., Chen, W., Hu, W., Li, W., Zhao, P., Cai, M., Peng, Y., Qi, J., Li, T., Wang, S., Chen, D., Yue, D., Yuan, B., and Shao, M.: Contrasting effects of secondary organic aerosol formations on organic aerosol hygroscopicity,

717 Atmospheric Chem. Phys., 21, 10375–10391, https://doi.org/10.5194/acp-21-10375-2021,
718 2021.

719 Lambe, A. T., Onasch, T. B., Massoli, P., Croasdale, D. R., Wright, J. P., Ahern, A. T.,
720 Williams, L. R., Worsnop, D. R., Brune, W. H., and Davidovits, P.: Laboratory studies of the
721 chemical composition and cloud condensation nuclei (CCN) activity of secondary organic
722 aerosol (SOA) and oxidized primary organic aerosol (OPOA), Atmospheric Chem. Phys., 11,
723 8913–8928, https://doi.org/10.5194/acp-11-8913-2011, 2011.

724 Liu, P., Song, M., Zhao, T., Gunthe, S. S., Ham, S., He, Y., Qin, Y. M., Gong, Z., Amorim, J.
725 C., Bertram, A. K., and Martin, S. T.: Resolving the mechanisms of hygroscopic growth and
726 cloud condensation nuclei activity for organic particulate matter, Nat. Commun., 9, 1–10,
727 https://doi.org/10.1038/s41467-018-06622-2, 2018.

728 Liu, P. F., Zhao, C. S., Göbel, T., Hallbauer, E., Nowak, A., Ran, L., Xu, W. Y., Deng, Z. Z.,
729 Ma, N., Mildenberger, K., Henning, S., Stratmann, F., and Wiedensohler, A.: Hygroscopic
730 properties of aerosol particles at high relative humidity and their diurnal variations in the
731 North China Plain, Atmospheric Chem. Phys., 11, 3479–3494, https://doi.org/10.5194/acp-
732 11-3479-2011, 2011.

733 Liu, X. and Wang, J.: How important is organic aerosol hygroscopicity to aerosol indirect
734 forcing?, Environ. Res. Lett., 5, 044010, https://doi.org/10.1088/1748-9326/5/4/044010,
735 2010.

736 Magi, B. I. and Hobbs, P. V.: Effects of humidity on aerosols in southern Africa during the
737 biomass burning season, J. Geophys. Res. Atmospheres, 108,
738 https://doi.org/10.1029/2002JD002144, 2003.

739 Mayer, K. J., Wang, X., Santander, M. V., Mitts, B. A., Sauer, J. S., Sultana, C. M., Cappa,
740 C. D., and Prather, K. A.: Secondary Marine Aerosol Plays a Dominant Role over Primary
741 Sea Spray Aerosol in Cloud Formation, ACS Cent. Sci., 6, 2259–2266,
742 https://doi.org/10.1021/acscentsci.0c00793, 2020.

743 Mei, F., Hayes, P. L., Ortega, A., Taylor, J. W., Allan, J. D., Gilman, J., Kuster, W., de
744 Gouw, J., Jimenez, J. L., and Wang, J.: Droplet activation properties of organic aerosols
745 observed at an urban site during CalNex-LA, J. Geophys. Res. Atmospheres, 118, 2903–
746 2917, https://doi.org/10.1002/jgrd.50285, 2013.

747 Mie, G.: Beiträge zur Optik trüber Medien, speziell kolloidaler Metallösungen, Ann. Phys.,
748 330, 377–445, https://doi.org/10.1002/andp.19083300302, 1908.

749 Petters, M. D. and Kreidenweis, S. M.: A single parameter representation of hygroscopic
750 growth and cloud condensation nucleus activity, Atmos Chem Phys, 11, 2007.

751 Petters, M. D., Carrico, C. M., Kreidenweis, S. M., Prenni, A. J., DeMott, P. J., Collett, J. L.,
752 and Moosmüller, H.: Cloud condensation nucleation activity of biomass burning aerosol, J.
753 Geophys. Res., 114, D22205, https://doi.org/10.1029/2009JD012353, 2009.

754 Quinn, P. K., Bates, T. S., Baynard, T., Clarke, A. D., Onasch, T. B., Wang, W., Rood, M. J.,
755 Andrews, E., Allan, J., Carrico, C. M., Coffman, D., and Worsnop, D.: Impact of particulate
756 organic matter on the relative humidity dependence of light scattering: A simplified
757 parameterization, Geophys. Res. Lett., 32, https://doi.org/10.1029/2005GL024322, 2005.

Rastak, N., Pajunoja, A., Acosta Navarro, J. C., Ma, J., Song, M., Partridge, D. G., Kirkevåg, A., Leong, Y., Hu, W. W., Taylor, N. F., Lambe, A., Cerully, K., Bougiatioti, A., Liu, P., Krejci, R., Petäjä, T., Percival, C., Davidovits, P., Worsnop, D. R., Ekman, A. M. L., Nenes, A., Martin, S., Jimenez, J. L., Collins, D. R., Topping, D. o., Bertram, A. K., Zuend, A., Virtanen, A., and Riipinen, I.: Microphysical explanation of the RH-dependent water affinity of biogenic organic aerosol and its importance for climate, Geophys. Res. Lett., 44, 5167–5177, https://doi.org/10.1002/2017GL073056, 2017.

Reddington, C. L., Morgan, W. T., Darbyshire, E., Brito, J., Coe, H., Artaxo, P., Scott, C. E., Marsham, J., and Spracklen, D. V.: Biomass burning aerosol over the Amazon: analysis of aircraft, surface and satellite observations using a global aerosol model, Atmospheric Chem. Phys., 19, 9125–9152, https://doi.org/10.5194/acp-19-9125-2019, 2019.

Redemann, J., Wood, R., Zuidema, P., Doherty, S. J., Luna, B., LeBlanc, S. E., Diamond, M. S., Shinozuka, Y., Chang, I. Y., Ueyama, R., Pfister, L., Ryoo, J.-M., Dobracki, A. N., da Silva, A. M., Longo, K. M., Kacenelenbogen, M. S., Flynn, C. J., Pistone, K., Knox, N. M., Piketh, S. J., Haywood, J. M., Formenti, P., Mallet, M., Stier, P., Ackerman, A. S., Bauer, S. E., Fridlind, A. M., Carmichael, G. R., Saide, P. E., Ferrada, G. A., Howell, S. G., Freitag, S., Cairns, B., Holben, B. N., Knobelspiesse, K. D., Tanelli, S., L'Ecuyer, T. S., Dzambo, A. M., Sy, O. O., McFarquhar, G. M., Poellot, M. R., Gupta, S., O'Brien, J. R., Nenes, A., Kacarab, M., Wong, J. P. S., Small-Griswold, J. D., Thornhill, K. L., Noone, D., Podolske, J. R., Schmidt, K. S., Pilewskie, P., Chen, H., Cochrane, S. P., Sedlacek, A. J., Lang, T. J., Stith, E., Segal-Rozenhaimer, M., Ferrare, R. A., Burton, S. P., Hostetler, C. A., Diner, D. J., Seidel, F. C., Platnick, S. E., Myers, J. S., Meyer, K. G., Spangenberg, D. A., Maring, H., and Gao, L.: An overview of the ORACLES (ObseRvations of Aerosols above CLouds and their intEractionS) project: aerosol–cloud–radiation interactions in the southeast Atlantic basin, Atmospheric Chem. Phys., 21, 1507–1563, https://doi.org/10.5194/acp-21-1507-2021, 2021.

Rickards, A. M. J., Miles, R. E. H., Davies, J. F., Marshall, F. H., and Reid, J. P.: Measurements of the Sensitivity of Aerosol Hygroscopicity and the κ Parameter to the O/C Ratio, J. Phys. Chem. A, 117, 14120–14131, https://doi.org/10.1021/jp407991n, 2013.

Sheridan, P. J., Jefferson, A., and Ogren, J. A.: Spatial variability of submicrometer aerosol radiative properties over the Indian Ocean during INDOEX, J. Geophys. Res. Atmospheres, 107, https://doi.org/10.1029/2000JD000166, 2002.

Shingler, T., Crosbie, E., Ortega, A., Shiraiwa, M., Zuend, A., Beyersdorf, A., Ziemba, L., Anderson, B., Thornhill, L., Perring, A. E., Schwarz, J. P., Campazano-Jost, P., Day, D. A., Jimenez, J. L., Hair, J. W., Mikoviny, T., Wisthaler, A., and Sorooshian, A.: Airborne characterization of subsaturated aerosol hygroscopicity and dry refractive index from the surface to 6.5 km during the SEAC4RS campaign, J. Geophys. Res. Atmospheres, 121, 4188–4210, https://doi.org/10.1002/2015JD024498, 2016.

Suda, S. R., Petters, M. D., Matsunaga, A., Sullivan, R. C., Ziemann, P. J., and Kreidenweis, S. M.: Hygroscopicity frequency distributions of secondary organic aerosols, J. Geophys. Res. Atmospheres, 117, https://doi.org/10.1029/2011JD016823, 2012.

Sumlin, B. J., Heinson, Y. W., Shetty, N., Pandey, A., Pattison, R. S., Baker, S., Hao, W. M., and Chakrabarty, R. K.: UV–Vis–IR spectral complex refractive indices and optical properties of brown carbon aerosol from biomass burning, J. Quant. Spectrosc. Radiat. Transf., 206, 392–398, https://doi.org/10.1016/j.jqsrt.2017.12.009, 2018.

802 Thompson, G. and Eidhammer, T.: A Study of Aerosol Impacts on Clouds and Precipitation
803 Development in a Large Winter Cyclone, J. Atmospheric Sci., 71, 3636–3658,
804 https://doi.org/10.1175/JAS-D-13-0305.1, 2014.

805 Titos, G., Cazorla, A., Zieger, P., Andrews, E., Lyamani, H., Granados-Muñoz, M. J., Olmo,
806 F. J., and Alados-Arboledas, L.: Effect of hygroscopic growth on the aerosol light-scattering
807 coefficient: A review of measurements, techniques and error sources, Atmos. Environ., 141,
808 494–507, https://doi.org/10.1016/j.atmosenv.2016.07.021, 2016.

809 Titos, G., Burgos, M. A., Zieger, P., Alados-Arboledas, L., Baltensperger, U., Jefferson, A.,
810 Sherman, J., Weingartner, E., Henzing, B., Luoma, K., O'Dowd, C., Wiedensohler, A., and
811 Andrews, E.: A global study of hygroscopicity-driven light-scattering enhancement in the
812 context of other in situ aerosol optical properties, Atmospheric Chem. Phys., 21, 13031–
813 13050, https://doi.org/10.5194/acp-21-13031-2021, 2021.

814 Wang, J., Shilling, J. E., Liu, J., Zelenyuk, A., Bell, D. M., Petters, M. D., Thalman, R., Mei,
815 F., Zaveri, R. A., and Zheng, G.: Cloud droplet activation of secondary organic aerosol is
816 mainly controlled by molecular weight, not water solubility, Atmospheric Chem. Phys., 19,
817 941–954, https://doi.org/10.5194/acp-19-941-2019, 2019.

818 Wang, W., Rood, M. J., Carrico, C. M., Covert, D. S., Quinn, P. K., and Bates, T. S.: Aerosol
819 optical properties along the northeast coast of North America during the New England Air
820 Quality Study–Intercontinental Transport and Chemical Transformation 2004 campaign and
821 the influence of aerosol composition, J. Geophys. Res. Atmospheres, 112,
822 https://doi.org/10.1029/2006JD007579, 2007.

823 van der Werf, G. R., Randerson, J. T., Giglio, L., Collatz, G. J., Mu, M., Kasibhatla, P. S.,
824 Morton, D. C., DeFries, R. S., Jin, Y., and van Leeuwen, T. T.: Global fire emissions and the
825 contribution of deforestation, savanna, forest, agricultural, and peat fires (1997–2009),
826 Atmospheric Chem. Phys., 10, 11707–11735, https://doi.org/10.5194/acp-10-11707-2010,
827 2010.

828 Wu, H., Taylor, J. W., Szpek, K., Langridge, J. M., Williams, P. I., Flynn, M., Allan, J. D.,
829 Abel, S. J., Pitt, J., Cotterell, M. I., Fox, C., Davies, N. W., Haywood, J., and Coe, H.:
830 Vertical variability of the properties of highly aged biomass burning aerosol transported over
831 the southeast Atlantic during CLARIFY-2017, Atmospheric Chem. Phys., 20, 12697–12719,
832 https://doi.org/10.5194/acp-20-12697-2020, 2020.

833 Zhang, L., Sun, J. Y., Shen, X. J., Zhang, Y. M., Che, H., Ma, Q. L., Zhang, Y. W., Zhang, X.
834 Y., and Ogren, J. A.: Observations of relative humidity effects on aerosol light scattering in
835 the Yangtze River Delta of China, Atmospheric Chem. Phys., 15, 8439–8454,
836 https://doi.org/10.5194/acp-15-8439-2015, 2015.

837 Zhang, L., Segal-Rozenhaimer, M., Che, H., Dang, C., Sedlacek III, A. J., Lewis, E. R.,
838 Dobracki, A., Wong, J. P. S., Formenti, P., Howell, S. G., and Nenes, A.: Light absorption by
839 brown carbon over the South-East Atlantic Ocean, Atmospheric Chem. Phys., 22, 9199–
840 9213, https://doi.org/10.5194/acp-22-9199-2022, 2022.

841 Zhang, Q., Jimenez, J. L., Canagaratna, M. R., Allan, J. D., Coe, H., Ulbrich, I., Alfarra, M.
842 R., Takami, A., Middlebrook, A. M., Sun, Y. L., Dzepina, K., Dunlea, E., Docherty, K.,
843 DeCarlo, P. F., Salcedo, D., Onasch, T., Jayne, J. T., Miyoshi, T., Shimono, A., Hatakeyama,

S., Takegawa, N., Kondo, Y., Schneider, J., Drewnick, F., Borrmann, S., Weimer, S., Demerjian, K., Williams, P., Bower, K., Bahreini, R., Cottrell, L., Griffin, R. J., Rautiainen, J., Sun, J. Y., Zhang, Y. M., and Worsnop, D. R.: Ubiquity and dominance of oxygenated species in organic aerosols in anthropogenically-influenced Northern Hemisphere midlatitudes, Geophys. Res. Lett., 34, https://doi.org/10.1029/2007GL029979, 2007.

Zieger, P., Fierz-Schmidhauser, R., Gysel, M., Ström, J., Henne, S., Yttri, K. E., Baltensperger, U., and Weingartner, E.: Effects of relative humidity on aerosol light scattering in the Arctic, Atmospheric Chem. Phys., 10, 3875–3890, https://doi.org/10.5194/acp-10-3875-2010, 2010.

Zieger, P., Fierz-Schmidhauser, R., Weingartner, E., and Baltensperger, U.: Effects of relative humidity on aerosol light scattering: results from different European sites, Atmospheric Chem. Phys., 13, 10609–10631, https://doi.org/10.5194/acp-13-10609-2013, 2013.

Zieger, P., Fierz-Schmidhauser, R., Poulain, L., Müller, T., Birmili, W., Spindler, G., Wiedensohler, A., Baltensperger, U., and Weingartner, E.: Influence of water uptake on the aerosol particle light scattering coefficients of the Central European aerosol, Tellus B Chem. Phys. Meteorol., 66, 22716, https://doi.org/10.3402/tellusb.v66.22716, 2014.

Zieger, P., Aalto, P. P., Aaltonen, V., Äijälä, M., Backman, J., Hong, J., Komppula, M., Krejci, R., Laborde, M., Lampilahti, J., de Leeuw, G., Pfüller, A., Rosati, B., Tesche, M., Tunved, P., Väänänen, R., and Petäjä, T.: Low hygroscopic scattering enhancement of boreal aerosol and the implications for a columnar optical closure study, Atmospheric Chem. Phys., 15, 7247–7267, https://doi.org/10.5194/acp-15-7247-2015, 2015.